Analytical Modeling of Residual Stress in Laser Powder Bed Fusion

Elham Mirkoohi[1,*], Jinqiang Ning[1], and Steven Y. Liang[1]

[1]Woodruff School of Mechanical Engineering, Georgia Institute of Technology, Atlanta, GA 30332, USA
*Corresponding author: Elham Mirkoohi, elham.mirkoohi@gatech.edu

Abstract

Rapid and accurate prediction of residual stress in metal additive manufacturing processes is of great importance to guarantee the quality of the fabricated part to be used in a mission-critical application in the aerospace and automotive industries. Experimentation and numerical modeling are valuable tools for measuring and predicting the residual stress; however, to-date conducting experimentation and numerical modeling is expensive and time-consuming. Thus, herein, a physics-based thermomechanical analytical model is proposed to predict the residual stress of the additively manufactured part rapidly and accurately. A moving point heat source approach is used to predict the temperature field by considering the effects of scan strategies, heat loss, and energy needed for solid-state phase transformation. Due to the high temperature gradient in this process, part experiences a high amount of thermal stress following solidification which may exceed the yield strength of the material. The thermal stress is obtained using Green's function of stresses due to the point body load. The Johnson-Cook flow stress model is used to predict the yield surface of the part under repeated heating and cooling. As a result of the cyclic heating and cooling and the fact that the material is yielded, the residual stress build-up is predicted based on incremental plasticity and kinematic hardening behavior of the metal according to the property of volume invariance in plastic deformation in coupling with the equilibrium and compatibility conditions. The computational methodology is realized with the laser powder fusion of maraging steel 350 as a material of example. The validation of the predictive models has been presented in terms of the comparison of predicted and measured scan-direction and build-direction residual stress distributions along depth of build under various process parameter combinations. Moreover, for the first time, the Jonson-Cook parameters of maraging steel 350 are predicted using analytical modeling of machining forces and non-linear optimization techniques.

Keywords: residual stress prediction; maraging steel 350; experimental measurement of residual stress

1. Introduction

Laser powder bed fusion (L-PBF) is a type of metal additive manufacturing (AM) process that produces metallic parts layer by layer via selectively melting the powders. In the past few years, L-PBF is utilized to manufacture a wide variety of parts and assemblies using a vast range of material systems [1]. Laser powder bed fusion process has several superiorities over conventional manufacturing processes including reduction in density, fabrication of more intricate parts than has been previously possible, a reduction in design and manufacturing time due to the single-step manufacturing, and many more [2]. Nevertheless, parts built via L-BPF usually contain a high level of residual stress due to the large temperature gradient and cooling rates [3]. This may cause the part to fail during or after fabrication due to the crack initiation and growth as caused by a high stress [4, 5]. Components produced via L-PBF are used in aerospace, automotive, medical, and marine industries, thus, high-quality components should be fabricated to be used in these critical

Preprints (www.preprints.org) | NOT PEER-REVIEWED | Posted: 23 January 2020 doi:10.20944/preprints202001.0268.v1

applications [1, 6]. An essential part of this qualification is the ability to accurately and rapidly predict the stress state within the part [7, 8].

There is significant work in literature on understanding and prediction of the residual stress formation during metal AM process under different process conditions [9]. This line of research can be categorized into three main parts. Experimental measurements, numerical modeling, and analytical modeling.

Residual stress measurements can be classified into destructive and non-destructive methods [10]. The popular non-destructive methods are X-ray diffraction and Neutron diffraction techniques which are capable of the surface and volumetric residual stress measurements, respectively [11, 12]. Destructive methods such as hole drilling, sectioning, and crack compliance are mainly revolved around creating free surfaces and relating the deformation to the resultant residual stresses. Wu *et al.* [13] measured the residual stress using the digital image correlation in conjunction with build plate removal and sectioning. The results are compared to the nondestructive volumetric neutron diffraction technique. They have concluded that the residual stress is reduced by decreasing the island size, increasing the applied energy per length, and increasing island to wall rotation to 45 degrees. Staub *et al*. [14] measured the residual stress using the X-ray technique in the L-PBF of SS316L. They have concluded that the higher aspect ratio (width/depth) of the melt pool geometry could result in higher residual stress. Wang *et al.* [15] used X-ray method to measure the residual stress from electron beam additive manufacturing (EBAM) process as well as the selective laser melting (SLM) for Ti-6Al-4V and IN718 parts. They have summarized that the residual stress of Ti-6Al-4V parts that are made using EBAM is more compressive compared to that made with IN-718. Also, the Ti-6Al-4V parts have a lower absolute value of the residual stress compared to IN718 parts.

Numerical modeling is another approach for the prediction of residual stress in metal AM. Hajializade *et al.* [16] performed a finite element (FE) simulation using an adaptive mesh coarsening algorithm to increase the computational efficiency of the FE model for the direct metal deposition (DMD) of the AISI 304L. They have used the double elliptical heat source model to predict the temperature distribution and used the result of thermal modeling to predict the residual stress. The heat loss due to the radiation is ignored in this modeling. Cheng *et al*. [17] performed FE modeling to predict the residual stress to design the support structure to mitigate residual stress formation. In this modeling, they have used the inherent strain method to decrease the computational time. Siewert *et al.* [18] predicted the residual stress by using the Mechanical Layer Equivalent (MLE) method to decrease the computational time. They have validated this model by measuring the residual stress using X-ray.

As explained before, there is significant research on the understanding of the residual stress formation under different process conditions using experimentations and finite element modeling. Experimental techniques to measure the residual stress within the part built via L-PBF certainly play an important role in the understanding of the residual stress formation. However, experimental measurement of the stress state in an entire part is time-consuming and expensive. Finite element models could predict the residual stress build-up in the AM components. However, performing FE simulations is challenged by the fact that it is computationally expensive. Consequently, many simplifications in modeling are conducted by applying different methods to predict the residual stress. While these simplifications are applied to this line of modeling, it still needs high-processor computers for the modeling of the entire process.

To circumvent the time demanding experimental repeated testing and finite element simulations, herein, a novel physics-based analytical model driven by computational mechanics of materials is

Preprints (www.preprints.org) | NOT PEER-REVIEWED | Posted: 23 January 2020 doi:10.20944/preprints202001.0268.v1

proposed to predict the residual stress in the parts built via L-PBF. The thermal signature of this process is predicted using a moving heat source approach by considering the scan strategy of the hatching space, layer thickness, and scan path, energy needed for solid-state phase change, and heat loss due to the convection and radiation. The high-temperature gradient and non-uniform heating in this process impose thermal stress on the component after solidification. The thermal stress is obtained by combining three sources of stresses known as stress due to the body forces, normal tension, and hydrostatic stress. Thermal stress may exceed the yield strength of the part. Hence, the Johnson-Cook (J-C) fellow stress model is used to predict the yield surface. For the first time, the J-C parameters of the maraging steel 350 (18Ni350) are predicted using a non-linear gradient search approach. As a result of repeated heating and cooling and the fact that the material is yielded, the through-thickness residual stress along the scan direction and build direction is predicted based on the incremental plasticity and kinematic hardening behavior of the metal according to the property of volume invariance in plastic deformation in coupling with equilibrium and compatibility conditions. It should be noted that the computational mechanics prediction presents a more time-efficient and resource-effective alternative to experimentations and finite element simulations as it does not involve repeated testing nor numerical iterations.

In this study, the physics-based prediction modeling methodology is implemented in the cased of laser powder bed fusion of maraging steel 350 (18Ni350 or M350) as a material of example. Maraging steel grade 350 is a popular alloy in the aerospace industry due to its superior strength and toughness without losing ductility. This class is a special class of low carbon ultra-high-strength steels that derive their strength not from the carbon but from the precipitation of intermetallic compounds [19]. Most high-strength steels have low toughness. The rare combination of high strength and toughness found within maraging steel makes it well suited for safety-critical aircraft structures that require high strength and damage tolerance. Maraging steel is strong, tough, low-carbon martensitic steel which contains hard precipitate particles formed by thermal aging [20]. Maraging steel 350 contains an extremely low carbon (0.03% maximum), and a large amount of nickel (18%) together with lesser amount of cobalt (12%), moleybdium (4%), titanium (1.5%) and aluminum (0.1%) [19].

The X-ray diffraction technique is used to measure the residual stress of the 18Ni350 components built via L-PBF to validate the proposed model. Good agreement is obtained between predicted and measured residual stress which indicates that the proposed model is a valuable tool for the rapid and accurate prediction of the residual stress build-up in the parts built via L-PBF. Due to the high computational efficiency of the proposed model, this model can also be used for the real-time monitoring and control of the build process, and also optimization of the process parameters in achieving a high-quality part.

2. Process Modeling

A physics-based closed-form analytical thermo-mechanical model is proposed to predict the residual stress in parts built via L-PBF. The high computational efficiency of the proposed model makes it a valuable tool for the prediction, control, and optimization of the L-PBF process to achieve a high-quality part by cutting the trial-and-error approach. This section goes into more detail regarding the specific thermal and mechanical model used.

Preprints (www.preprints.org) | NOT PEER-REVIEWED | Posted: 23 January 2020 doi:10.20944/preprints202001.0268.v1

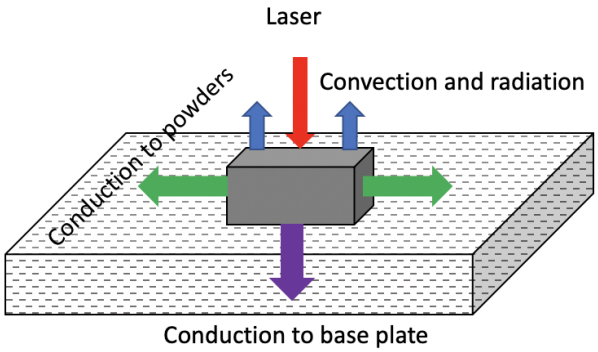

Figure 1. *Heat transfer mechanisms in laser powder bed fusion.*

2.1 Thermal Modeling

A moving point heat source approach is used to predict the temperature field within the parts built via L-PBF. The initial solution of temperature in a semi-infinite medium is derived by Carslaw and Jaeger [21]. Heat losses at part's boundaries including conduction on lateral faces and convection and radiation on the top surface are solved by modifying the heat source solution. Figure 1 illustrates the heat transfer mechanisms in L-PBF. The closed-form solution of temperature considering part's boundary condition can be obtained as;

$$T = \frac{P\alpha}{4\pi KR}\exp\left(-\frac{V(x+R)}{2D}\right) - A\sum_{i=1}^{n}\frac{h(T_i - T_0) + \varepsilon\sigma\left({T_i}^4 - {T_0}^4\right)}{4\pi KR} + T_0 \quad (1)$$

where P is the laser power, α represents absorption coefficient, K is the thermal conductivity, $R = \sqrt{x^2 + y^2 + z^2}$ is the radial distance from heat source, V is the laser speed, $D = \frac{K}{\rho C}$ is the thermal diffusivity, ρ is density, C is the specific heat, A is the area of the heat sink, h is convection coefficient, ε is emissivity, σ is Stefan-Boltzmann constant, n is the number of heat sinks, i is the index of each heat sink, and T_0 is the initial temperature. More explanation about the heat source solution can be obtained from the previous work of these authors in [22-25].

2.2 Thermal Stress Prediction

Non-uniform heating induced by fast irradiation of the laser and relatively low conduction, re-melting and re-solidification, and different thermal expansion coefficient induced by steep temperature gradient throughout the part are the main sources of thermal stress [25, 26].

Accordingly, the thermal stress due to the non-uniform heating in the build part could be obtained using Green's function of stresses due to the point body load. The obtained thermal stress is the combination of stresses due to the body forces, normal tension, and hydrostatic stress as described by Saif *et al.* [27]:

Preprints (www.preprints.org) | NOT PEER-REVIEWED | Posted: 23 January 2020 doi:10.20944/preprints202001.0268.v1

$$\sigma_{xx}(x,z) = -\frac{\alpha(T)E(T)}{1-2\nu(T)}\int_0^\infty\int_{-\infty}^\infty (G_{xh}\frac{\partial T}{\partial x}(x',z') + G_{xv}\frac{\partial T}{\partial z}(x',z'))dx'dz' + \frac{2z}{\pi}\int_{-\infty}^\infty \frac{p(s)(s-x)^2}{((s-x)^2+z^2)^2}ds - \frac{\alpha(T)E(T)T(x,z)}{1-2\nu(T)} \quad (2)$$

$$\sigma_{zz}(x,z) = -\frac{\alpha(T)E(T)}{1-2\nu(T)}\int_0^\infty\int_{-\infty}^\infty (G_{zh}\frac{\partial T}{\partial x}(x',z') + G_{zv}\frac{\partial T}{\partial z}(x',z'))dx'dz' + \frac{2z^3}{\pi}\int_{-\infty}^\infty \frac{p(s)}{((s-x)^2+z^2)^2}ds - \frac{\alpha(T)E(T)T(x,z)}{1-2\nu(T)} \quad (3)$$

$$\sigma_{xz}(x,z) = -\frac{\alpha(T)E(T)}{1-2\nu(T)}\int_0^\infty\int_{-\infty}^\infty (G_{xzh}\frac{\partial T}{\partial x}(x',z') + G_{xzv}\frac{\partial T}{\partial z}(x',z'))dx'dz' + \frac{2z^2}{\pi}\int_{-\infty}^\infty \frac{p(s)(s-x)}{((s-x)^2+z^2)^2}ds \quad (4)$$

$$\sigma_{yy}(x,z) = \nu(T)(\sigma_{xx}+\sigma_{zz}) - \alpha(T)E(T)T(x,z) \quad (5)$$

where, α represents the coefficient of the thermal expansion, E is the elastic modulus, $\frac{\partial T}{\partial x}$ is the temperature gradient and $p(s)$ is expressped by:

$$p(s) = \frac{\alpha(T)E(T)T(x,z=0)}{1-2\nu(T)} \quad (6)$$

$(G_{xh}, G_{xV}, G_{zh}, G_{zv}, G_{xzh,}G_{xzv})$ are the plane strain Green's function which explained in appendix A.

The closed-form solution of thermal stress can be derived as;

$$\sigma_{xx}(i,j) = -\frac{\alpha E(T)}{1-2\nu}\left(G_{xh}T_x + G_{xv}T_z\right)\left(|x_i - x_{i-1}||z_j - z_{j-1}|\right) + \frac{\frac{2z}{\pi}(p(s)(s-x)^2}{((s-x)^2+z^2)^2}|x_i - x_{i-1}| - \frac{\alpha ET}{1-2\nu} \quad (7)$$

where $T_x = \frac{T(i,j)-\mathrm{T(i-1,j)}}{|x_i-x_{i-1}|}$, $T_z = \frac{T(i,j)-\mathrm{T(i,j-1)}}{|z_j-z_{j-1}|}$ and i, j represent a location in the 2D medium at which the stress is calculated. The closed-form solutions of σ_{zz} and σ_{xz} can be derived using the same method.

2.3 Residual Stress Prediction

The Johnson-Cook (J-C) flow stress model is employed to determine the yield surface of the material as;

Preprints (www.preprints.org) | NOT PEER-REVIEWED | Posted: 23 January 2020 doi:10.20944/preprints202001.0268.v1

$$\sigma = (A + B{\varepsilon_{eff}^{p}}^{n})(1 + Cln\left(\frac{\dot{\varepsilon}_{eff}^{p}}{\dot{\varepsilon}_0}\right))(1 - \left[\frac{T - T_0}{T_m - T_0}\right]^{m}) \tag{8}$$

where ε_{eff}^{p} is the effective plastic strain, $\dot{\varepsilon}_{eff}^{p}$ is the effective plastic strain rate, T is the temperature of material, T_m is the melting point of material, and T_0 is the initial temperature. The terms A, B, C, n, m and $\dot{\varepsilon}_0$ are the material constant for 18Ni350. To the best of our knowledge, there is no data for the J-C parameters of 18Ni350 on literature. Thus, a physics-based inverse analytical model is employed to predict the J-C parameters as explained in section 3.1.
The effective plastic strain and strain rate are defined as;

$$\varepsilon_{eff}^{p} = \frac{\sqrt{2}}{3}\sqrt{(\varepsilon_{xx}^{p} - \varepsilon_{yy}^{p})^2 + (\varepsilon_{yy}^{p} - \varepsilon_{zz}^{p})^2 + (\varepsilon_{zz}^{p} - \varepsilon_{xx}^{p})^2 + 6(\varepsilon_{xz}^{p})^2} \tag{9}$$

$$\dot{\varepsilon}_{eff}^{p} = \sqrt{\frac{2}{3}}\sqrt{(\dot{\varepsilon}_{xx}^{p})^2 + (\dot{\varepsilon}_{yy}^{p})^2 + (\dot{\varepsilon}_{zz}^{p})^2 + (\dot{\varepsilon}_{xz}^{p})^2} \tag{10}$$

The yielding criterion is obtained for an isotropic material. Kinematic hardening is considered by employing backstress tensor (α_{ij})

$$F_{yield} = \frac{3}{2}(S_{ij} - \alpha_{ij})(S_{ij} - \alpha_{ij}) - k^2 = 0 \tag{11}$$

$$\begin{cases} F_{yield} < 0 \; elastic \; deformation \\ F_{yield} > 0 \; plastic \; deformation \end{cases}$$

where $S_{ij} = \sigma_{ij} - ({}^{\sigma_{kk}}/_{3})\delta_{ij}$ is the deviatoric stress. The material yield threshold which is determined using material flow stress model can be obtained as

$$k = \frac{1}{\sqrt{3}}(A + B{\varepsilon_{eff}^{p}}^{n})(1 + Cln\left(\frac{\dot{\varepsilon}_{eff}^{p}}{\dot{\varepsilon}_0}\right))(1 - \left[\frac{T - T_0}{T_m - T_0}\right]^{m}) \tag{12}$$

$\dot{\alpha_{ij}} = \langle \dot{S_{kl}} n_{kl} \rangle n_{ij}$ shows the evolution of back stress tensor in linear kinematic hardening, where $<>$ is MacCauley bracket and is defined as $\langle x \rangle = 0.5(x + |x|)$, and $n_{ij} = \frac{S_{ij} - \alpha_{ij}}{\sqrt{2}\,k}$ which is the components of unit normal in plastic strain rate direction (on yield surface), and k is the material flow stress threshold.
Elasticity module and yield strength are considered temperature dependent, which force the model to be updated incrementally. If $F_{yield} < 0$, material is in elastic region and the stresses can be obtained from the Hook's Law.

Preprints (www.preprints.org) | NOT PEER-REVIEWED | Posted: 23 January 2020 doi:10.20944/preprints202001.0268.v1

If $F_{yield} > 0$, incremental plastic strains are calculated and accumulated during the stress history to determine the total plastic strains. Plastic strain is irreversible and path dependent, consequently, the governing equations should be written in the form of differential equations. The plastic strain rate is determined by Khan and Huang [28] as

$$\dot{\varepsilon}_{ij}^{P} = \frac{1}{h}\langle \dot{S_{kl}} n_{kl} \rangle n_{ij} \tag{13}$$

where h is the plastic modulus. In the elastic-plastic case where the $F_{yeild} \geq 0$, the strain rate along the scan direction and transverse direction can be calculated using modified McDowell algorithm [29].

$$\begin{cases} \frac{1}{E}\left[\dot{\sigma}_{xx} - \upsilon\left(\dot{\sigma}_{yy} - \dot{\sigma}_{zz}\right)\right] + \alpha\Delta T + \frac{1}{h}\left(\dot{\sigma}_{xx}n_{xx} + \dot{\sigma}_{yy}n_{yy} + \dot{\sigma}_{zz}n_{zz} + 2\dot{\sigma}_{xz}^{*}n_{xz}\right)n_{xx} = \\ \psi\left(\frac{1}{E}\left[\dot{\sigma}_{xx}^{*} - \upsilon\left(\dot{\sigma}_{yy} - \dot{\sigma}_{zz}^{*}\right)\right] + \alpha\Delta T + \frac{1}{h}\left(\dot{\sigma}_{xx}^{*}n_{xx} + \dot{\sigma}_{yy}n_{yy} + \dot{\sigma}_{zz}^{*}n_{zz} + 2\dot{\sigma}_{xz}^{*}n_{xz}\right)n_{xx}\right) \\ \frac{1}{E}\left[\dot{\sigma}_{yy} - \upsilon(\dot{\sigma}_{xx} - \dot{\sigma}_{zz})\right] + \alpha\Delta T + \frac{1}{h}\left(\dot{\sigma}_{xx}n_{xx} + \dot{\sigma}_{yy}n_{yy} + \dot{\sigma}_{zz}n_{zz} + 2\dot{\sigma}_{xz}^{*}n_{xz}\right)n_{yy} = 0 \\ \dot{\sigma}_{yy} = \frac{1}{2}(\dot{\sigma}_{xx} + \dot{\sigma}_{zz}) \end{cases} \tag{14}$$

where, $\dot{\sigma}_{xx}^{*}, \dot{\sigma}_{zz}^{*}, \dot{\sigma}_{xz}^{*}$ are the elastic thermal stresses calculated from Equations (2 and 6). In McDowell model, a hybrid function (ψ) is proposed, which depends on the instantaneous value of the modulus ratio h/G as;

$$\psi = 1 - \exp\left(-\xi\frac{3h}{2G}\right) \tag{15}$$

where $\xi = 0.2$ is the algorithm constant which is determined by the comparison of the finite element and analytical modeling results [30], h is the plastic modulus, and $G = E/(2(1+\upsilon))$is the elastic shear modulus. ψ approaches zero as h approaches zero (perfect plasticity), and ψ approaches unity as h approaches infinity (initial yielding). ψ is always between unity and zero. Three systems of equations are solved simultaneously for $\dot{\sigma}_{xx}$, $\dot{\sigma}_{yy}$, and $\dot{\sigma}_{zz}$ for each elastic-plastic increment of strain.

2.4 Stress Relaxation

After laser scanned one layer, elastic stresses are relaxed to satisfy the boundary condition prescribed by Merwin and Johnson [31] as

$$\varepsilon_{xx}^{r} = 0, \quad \sigma_{xx}^{r} = f_1(z), \quad \varepsilon_{yy}^{r} = 0, \quad \sigma_{yy}^{r} = f_2(z), \quad \varepsilon_{zz}^{r} = f_3(z), \quad \sigma_{zz}^{r} = 0,$$

$$\gamma_{xz}^{r} = f_4(z), \qquad \sigma_{xz}^{r} = 0 \tag{16}$$

Preprints (www.preprints.org) | NOT PEER-REVIEWED | Posted: 23 January 2020 doi:10.20944/preprints202001.0268.v1

Finally, only stresses and strains parallel to the surface (σ_{xx}^r, $\sigma_{yy}^r, \gamma_{xz}^r$) remain non-zero. The only non-zero strain is ε_{zz}^r, resulting from surface compression. Accordingly, the non-zero components $\varepsilon_{xx}^r, \sigma_{zz}^r,$ and σ_{xz}^r at the end of each pass should incrementally relax to zero as;

$$\Delta\sigma_{zz} = -\frac{\sigma_{zz}^r}{M}, \Delta\sigma_{xz} = -\frac{\sigma_{xz}^r}{M}, \Delta\varepsilon_{xx} = -\frac{\varepsilon_{xx}^r}{M} \tag{17}$$

where M is the number of increments (e.g.100-1000) taken into the relaxation process to relax the non-zero components ($\varepsilon_{xx}^r, \sigma_{zz}^r,$ and σ_{xz}^r) to zero.

Using Equation (16), for the case of purely elastic relaxation increment ($F_{yeild} \leq 0$), the relaxation process is described by general Hook's law as

$$\begin{cases} \Delta\sigma_{xx} = \dfrac{E\Delta\varepsilon_{xx} + (1+\upsilon)(\Delta\sigma_{zz}\upsilon - E\alpha\Delta T)}{(1-\upsilon^2)} \\ \Delta\sigma_{yy} = \dfrac{\upsilon E\Delta\varepsilon_{xx} + (1+\upsilon)(\Delta\sigma_{zz}\upsilon - E\alpha\Delta T)}{(1-\upsilon^2)} \end{cases} \tag{18}$$

$\Delta's$ replaces the time derivative.

For the elastic-plastic case ($F_{yeild} > 0$), the released stresses calculated as

$$\begin{cases} \Delta\sigma_{xx} = \dfrac{D - \left(\frac{1}{E} + \frac{1}{h}n_{xx}n_{yy}\right)\Delta\sigma_{yy} - \alpha\Delta\mathrm{T}}{-\frac{\upsilon}{E} + \frac{1}{h}n_{xx}n_{yy}} \\ \Delta\sigma_{yy} = \dfrac{(-\frac{\upsilon}{E} + \frac{1}{h}n_{xx}n_{yy})(C - \alpha\Delta\mathrm{T}) - (\frac{1}{E} + \frac{1}{h}n_{xx}n_{xx})(D - \alpha\Delta\mathrm{T})}{\left[(-\frac{\upsilon}{E} + \frac{1}{h}n_{xx}n_{yy})^2 - (\frac{1}{E} + \frac{1}{h}n_{xx}n_{xx})(\frac{1}{E} + \frac{1}{h}n_{yy}n_{yy})\right]} \end{cases} \tag{19a, b}$$

$$\text{where} \begin{cases} C = \Delta\varepsilon_{xx} + \left(\frac{\upsilon}{E} - \frac{1}{h}n_{xx}n_{zz}\right)\Delta\sigma_{zz}{}^* - \frac{2}{h}\,\Delta\sigma_{xz}{}^* n_{xz}n_{xx} \\ D = \left(\frac{\upsilon}{E} - \frac{1}{h}n_{yy}n_{zz}\right)\Delta\sigma_{zz}{}^* - \frac{2}{h}\,\Delta\sigma_{xz}{}^* n_{xz}n_{yy} \end{cases} \tag{20}$$

The residual stresses in the scan direction and build direction are then calculated as the remaining stresses after relaxation.

3. Prediction of Johnson-Cook (J-C) Parameters

Since the J-C parameters of 18Ni350 are not reported in the literature, herein, an inverse analytical model is employed to predict the J-C parameters of 18Ni350 using modified machining chip formation model and gradient search method. In this approach, the modified chip formation model is used to predict the machining forces, and the iterative gradient search is used to determine the J-C parameters when the difference between predicted and measured cutting forces is below an acceptable low value. More detail about the modeling can be found in [32]. The predicted J-C parameters for 18Ni350 are listed in Table 1.

Preprints (www.preprints.org) | NOT PEER-REVIEWED | Posted: 23 January 2020 doi:10.20944/preprints202001.0268.v1

Table 1. *Johnson-Cook parameters of 18Ni350.*

A [MPa]	B [MPa]	C	n	m
830	1067	0.028	0.107	0.7

4. Experimental Validation

4.1. Build Printing Process

A Truprint 1000 selective laser melting (SLM) machine, equipped with a 200W YAG laser is used to fabricate rectangular bar shape maraging steel 350 samples with dimensions of $10 \times 5 \times 10\ mm^3$. Density of the additively manufactured part built via L-PBF has a crucial impact on mechanical properties of the fabricated component. An approach to identify processing parameters for producing high-density parts is employed to select the processing conditions as described in the previous studies [33-36]. The processing conditions used to fabricate high-density samples for measuring the residual stress are listed in Table 2. The spherical 18Ni350 powders used in this study are distributed between 15 µm to 45 µm. The process parameters are selected in a way to capture the effects of scan speed and laser power on residual stress, thus the other parameters of layer thickness, hatching space, and hatch style are kept the same for all the samples. The composition of the 18Ni350 is listed in Table 3. Figure 2 illustrates the as-build samples and were then removed from the base plate using the electrical discharge machining (EDM).

Table 2. *Process Parameters Designed for the fabrication of 18Ni350 specimens using L-PBF.*

Sample	**Laser power (W)**	**Scan speed (mm/s)**	**Layer thickness (µm)**	**Hatching space (µm)**	**Hatch style**
1	120	100	45	100	zig-zag unconnected
2	180	100	45	100	zig-zag unconnected
3	120	200	45	100	zig-zag unconnected

Table 3. *Compositions of 18Ni350 steels powder*

wt%	Fe	Ni	Co	Mo	Ti	Al	Cr
18Ni350	Bal	18.77	12.09	4.78	1.31	0.14	0.12
wt%	Si	Mn	S	B	P	C	Cu
18Ni350	0.02	0.09	0.003	<0.001	0.007	0.01	0.2

Preprints (www.preprints.org) | NOT PEER-REVIEWED | Posted: 23 January 2020 doi:10.20944/preprints202001.0268.v1

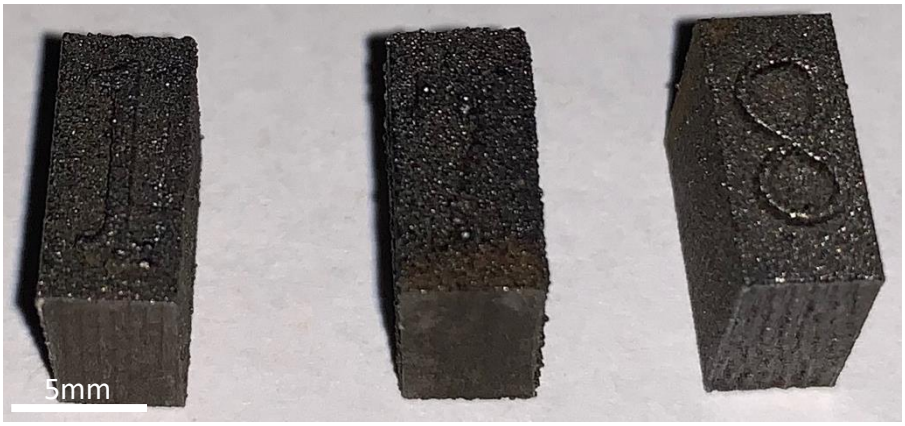

Figure 2. *Illustration of the as-build 18Ni350 parts manufactured via L-PBF.*

4.2 Experimental Measurement of Residual Stress

The residual stress on the side walls of the samples, as illustrated in Figure 3 was measured by a commercial X-Ray Diffractions machine (D8 Discover Bruker) using the $sin^2\Psi$ method [37, 38]. The coordinate and location of measured points are shown in Table 4. For each point shown in Figure 4, the through-thickness residual stresses along the build direction (*z*-direction), and along the scan direction (*x*-direction) were measured. The parameters for XRD measurement are specified in Table 5. It is noted that for each set of parameters and each point shown in Figure 4, the XRD measurements were performed on two fabricated samples, two times and the results were averaged.

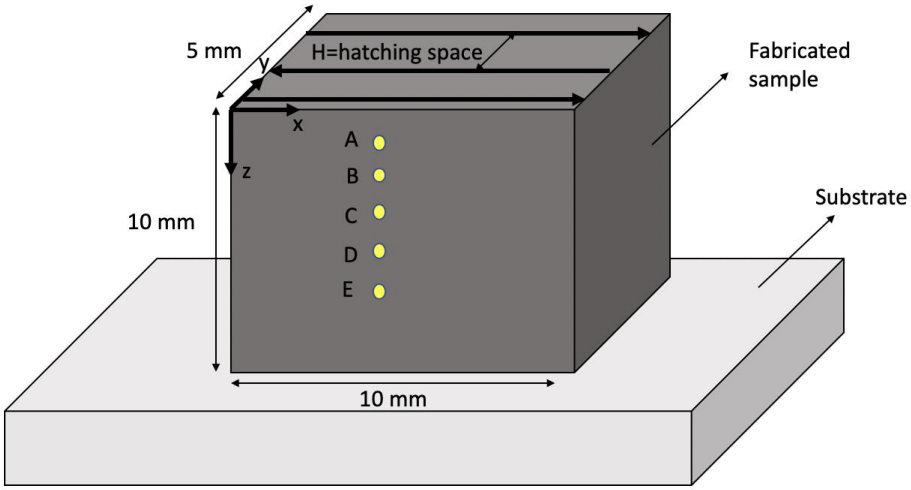

Figure 3. *Schematic diagram illustrating the definition of processing parameters*

Table 4. *Coordinates of the measured points using XRD.*

A	x = 5 mm; y = 0; z = 0.5 mm
B	x = 5 mm; y = 0; z = 1.5 mm

Preprints (www.preprints.org) | NOT PEER-REVIEWED | Posted: 23 January 2020 doi:10.20944/preprints202001.0268.v1

C	x = 5 mm; y = 0; z = 2.5 mm
D	x = 5 mm; y = 0; z = 3.5 mm
E	x = 5 mm; y = 0; z = 4.5 mm

Table 5. *Parameters for XRD measurements*

Focus	1.0 mm
Radiation	Cu Kα
Lattice plane (hkl)	{211}
2Θ	145 º
Ψ-tilting	0º to 45º in 6 steps each
Young modulus	190 GPa
Poisson ration	0.3

5. Results and Discussion

The proposed thermomechanical analytical model enables the prediction of the residual stress of the fabricated L-PBF samples under different process conditions along the scan direction (σ_{xx}) and build direction (σ_{zz}). The thermomechanical material properties of the 18Ni350 are listed in Table 6. The thermal response of the build part is predicted using moving point heat source approach by considering the effects of heat loss due to the convection and radiation, scan strategies, and energy needed for solid-state phase transformation. Figures 4 to 6 illustrate the predicted temperature field for three 18Ni350 samples listed in Table 2. The analytical modeling of the temperature field is validated in the previous work of authors [22].

Table 6. *Thermo-mechanical material properties of Maraging steel 350 [39].*

Density [g/cm^3]	Thermal conductivity [W/m°C]	Specific heat [J/kg°C]	Thermal expansion [μm/m°C]	Elastic modulus [GPa]	Poisson's ratio	Melting onset [°C]	Liquidus Temperature [°C]	Latent Heat of fusion [J/g]
8.2	14.75	450	12	190	0.3	1420	1470	270

Figure 4 demonstrates the predicted temperature field for the first sample with the laser power of 120 W, scan speed of 100 mm/s, layer thickness of 45 μm, hatching space of 100 μm, and scan pattern of unconnected zigzag. Figure 5 illustrates the predicted temperature field for the second sample with the laser power of 180 W, scan speed of 100 mm/s, layer thickness of 45 μm, hatching space of 100 μm, and scan pattern of unconnected zigzag. And, Figures 6 depicts the predicted temperature field for the third sample with the laser power of 120 W, scan speed of 200 mm/s, layer thickness of 45 μm, hatching space of 100 μm, and scan pattern of unconnected zigzag.
Comparison of the Figures 4 and 5 shows that the increase in laser power would increase the melt pool area, and the comparison of Figure 4 and 6 illustrates that for the same laser power the increase in scan speed would decrease the melt pool geometry which is a very well-known knowledge and

Preprints (www.preprints.org) | NOT PEER-REVIEWED | Posted: 23 January 2020 doi:10.20944/preprints202001.0268.v1

confirms that the proposed model properly follows the trend. The proposed analytical model of the temperature field is validated in the previous work of these authors.

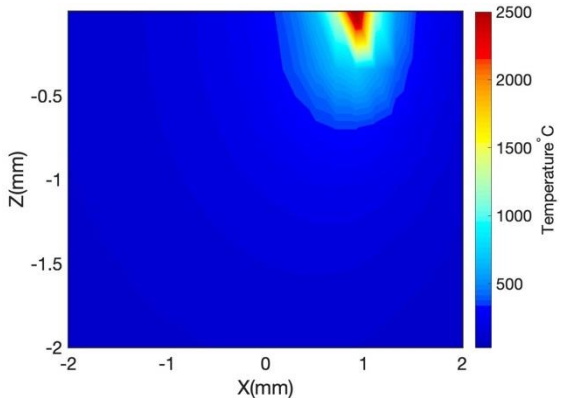

Figure 4. *Predicted temperature field for the fabricated Maraging steel 350 sample built via L-PBF with the laser power of 120 W and scan speed of 100 mm/s, layer thickness of 45 µm, hatching space of 100 µm, and scan pattern of unconnected zigzag.*

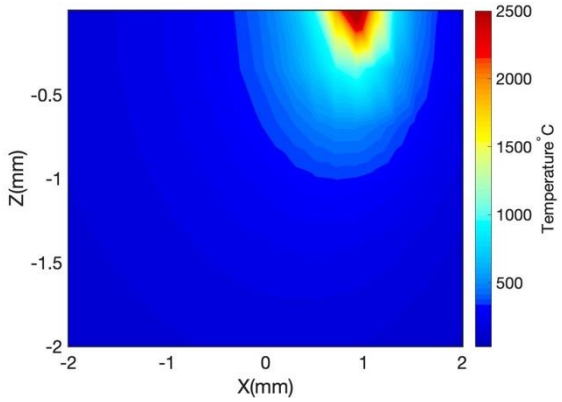

Figure 5. *Predicted temperature field for the fabricated Maraging steel 350 sample built via L-PBF with the laser power of 180 W and scan speed of 100 mm/s, layer thickness of 45 µm, hatching space of 100 µm, and scan pattern of unconnected zigzag.*

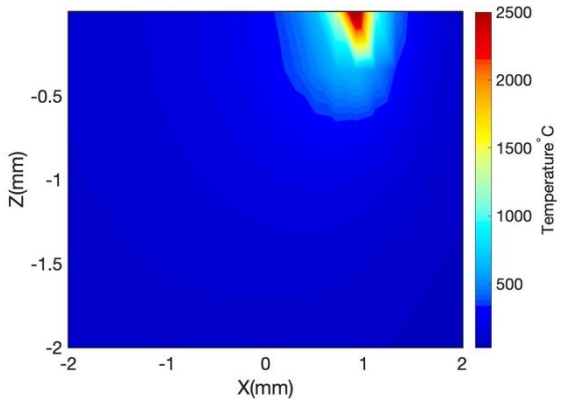

Preprints (www.preprints.org) | NOT PEER-REVIEWED | Posted: 23 January 2020 doi:10.20944/preprints202001.0268.v1

Figure 6. *Predicted temperature field for the fabricated Maraging steel 350 sample built via L-PBF with the laser power of 120 W and scan speed of 200 mm/s, layer thickness of 45 µm, hatching space of 100 µm, and scan pattern of unconnected zigzag.*

High-temperature gradient and fast cooling rate induce thermal stress in the fabricated part. The thermal stress is calculated using Green's function of stresses due to the point body load. The thermal stress is a combination of three main sources of stress known as stresses due to body forces, normal tension, and hydrostatic stress. The thermal stress may exceed the yield strength of the material. The yield surface is predicted using the J-C flow stress model. Due to the repeated heating and cooling and the fact that the material is yielded the part experiences a high level of residual stress. Residual stress is calculated using incremental plasticity and kinematic hardening behavior of the material in coupling with equilibrium and compatibility conditions.
Figures 7 through 9 illustrate the predicted thermal stress along the build direction and scan direction for three maraging steel 350 samples. It is observed that the thermal stress along the build direction is higher than that along the scan direction due to the difference in temperature gradient in different directions. Also, the predicted thermal stress along the build direction is more tensile compared to that in the scan direction due to the same reason. The thermal stress model is validated in the previous work of authors which is currently under review.

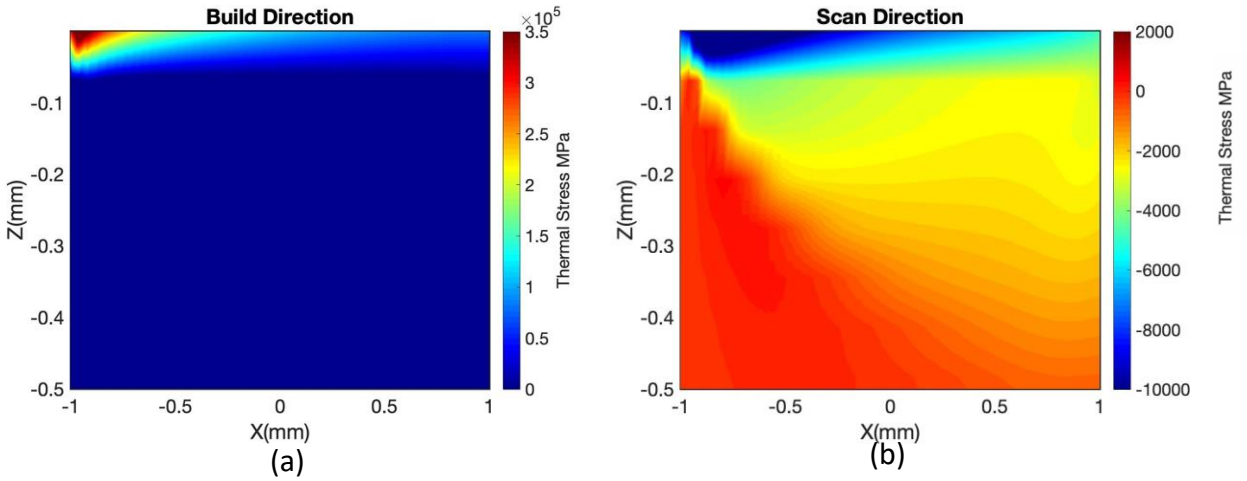

Figure 7. *Predicted thermal stress for the fabricated Maraging steel 350 sample built via L-PBF with the laser power of 120 W and scan speed of 100 mm/s, layer thickness of 45 µm, hatching space of 100 µm, and scan pattern of unconnected zigzag; (a) along build direction; (b) along scan direction.*

Preprints (www.preprints.org) | NOT PEER-REVIEWED | Posted: 23 January 2020 doi:10.20944/preprints202001.0268.v1

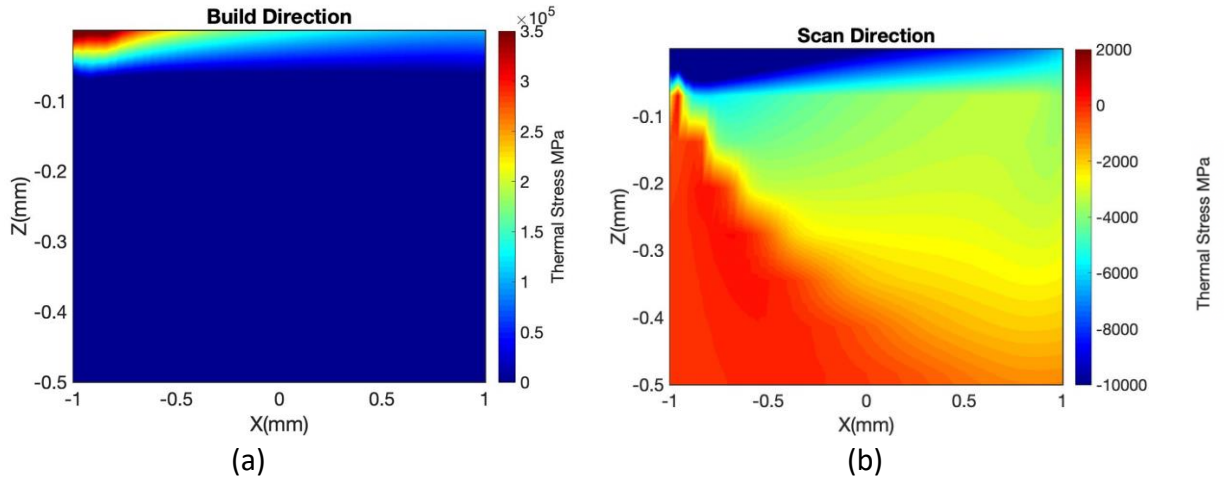

Figure 8. *Predicted thermal stress for the fabricated Maraging steel 350 sample built via L-PBF with the laser power of 180 W and scan speed of 100 mm/s, layer thickness of 45 μm, hatching space of 100 μm, and scan pattern of unconnected zigzag; (a) along build direction; (b) along scan direction*

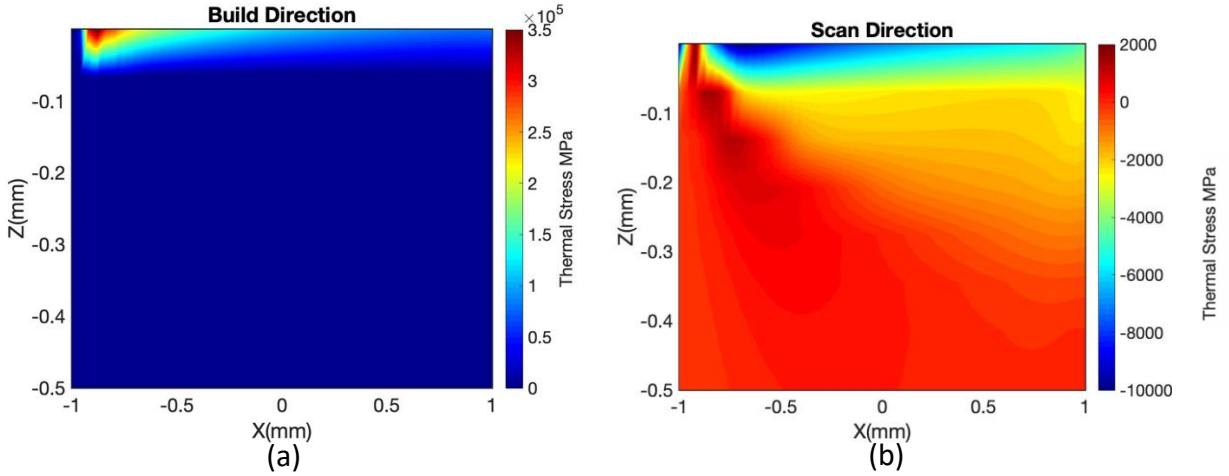

Figure 9. *Predicted thermal stress for the fabricated Maraging steel 350 sample built via L-PBF with the laser power of 120 W and scan speed of 200 mm/s, layer thickness of 45 μm, hatching space of 100 μm, and scan pattern of unconnected zigzag; (a) along build direction; (b) along scan direction.*

Figures 10 (a & b) illustrate the predict residual stress for the 18Ni350 sample which is built with the laser power of 120 W, scan speed of 100 mm/s, layer thickness of 45 μm, hatching space of 100 μm, and scan pattern of unconnected zigzag. The residual stress is predicted along the scan direction and build direction. The predicted residual stress is compared to the experimental measurement of the residual stress 18Ni350 sample. The residual stress is measured at four different locations through the thickness as shown in Figure 3. The predicted and measured residual stress are highly compressive along both scan direction and build direction since during the cooling cycle the heat-affected zone begins to cool down and the shrinkage of material in this zone tend to occur, but the shrinkage is restrained by the plastic strain formed during the heating stage, thus, the compressive stress state builds up in the solidified part. Moreover, the predicted and measured residual stress along the build direction showed higher value compare to that along the scan direction, this is due to the fact that the heat transfer mechanism varies in different directions and would result in different temperature gradient and cooling rates [40].

Preprints (www.preprints.org) | NOT PEER-REVIEWED | Posted: 23 January 2020 doi:10.20944/preprints202001.0268.v1

Figures 11(a & b) demonstrate the predicted and measured residual stress of 18Ni350 sample with the laser power of 180 W, scan speed of 100 mm/s, layer thickness of 45 μm, hatching space of 100 μm, and scan pattern of unconnected zigzag. The predicted residual stress along the scan direction and build direction are highly compressive in accordance with the data in the literature. Furthermore, the predicted residual stress along the scan direction has lower value compared to that along the build direction. As explained before, different heat transfer mechanisms contribute to this variation.

Figures 12(a & b) show the predicted and measured residual stress along the scan direction and build direction for the laser power of 120 W, scan speed of 200 mm/s, layer thickness of 45 μm, hatching space of 100 μm, and scan pattern of unconnected zigzag. As shown in these figures, the predicted residual stress is highly compressive along the scan direction and build direction. The predicted residual stress showed good agreement with measured residual stress of 18Ni350.

To sum it up, the comparison of the predicted and measured residual stress for three 18Ni350 samples showed that the proposed thermo-mechanical computational mechanics model can predict the residual stress of the additively manufactured part accurately. Therefore, the proposed model is a valuable, reliable, and rapid tool for the prediction of stress state within the part which then can be used for the optimization of process parameters and control of the build process. It should be noted that the proposed model works for all the material systems as long as the thermo-mechanical material properties are known.

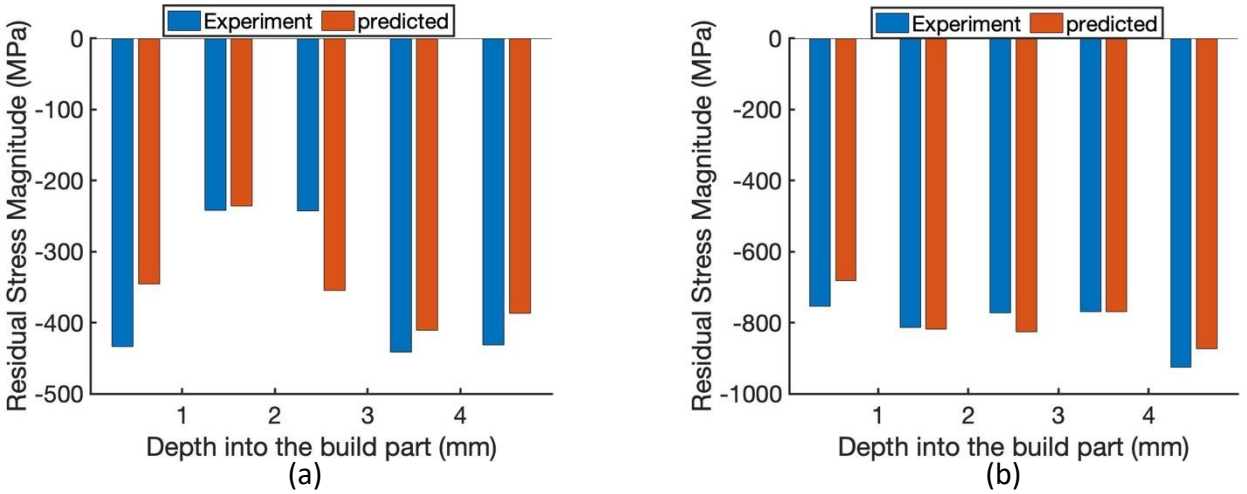

Figure 10. *Predicted and measured residual stress of 18Ni350 sample built via L-PBF with the laser power of 120 W and scan speed of 100 mm/s, layer thickness of 45 µm, hatching space of 100 µm, and scan pattern of unconnected zigzag; (a) along the scan direction ; (b) along the build direction.*

Preprints (www.preprints.org) | NOT PEER-REVIEWED | Posted: 23 January 2020 doi:10.20944/preprints202001.0268.v1

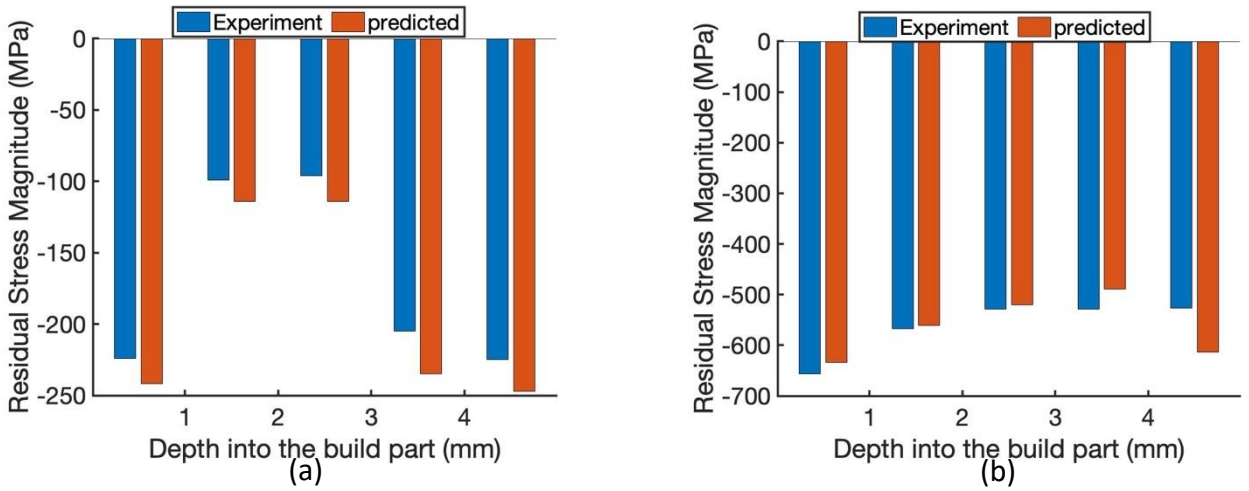

Figure 11. *Predicted and measured residual stress of 18Ni350 sample built via L-PBF with the laser power of 180 W and scan speed of 100 mm/s, layer thickness of 45 µm, hatching space of 100 µm, and scan pattern of unconnected zigzag; (a) along the scan direction ; (b) along the build direction.*

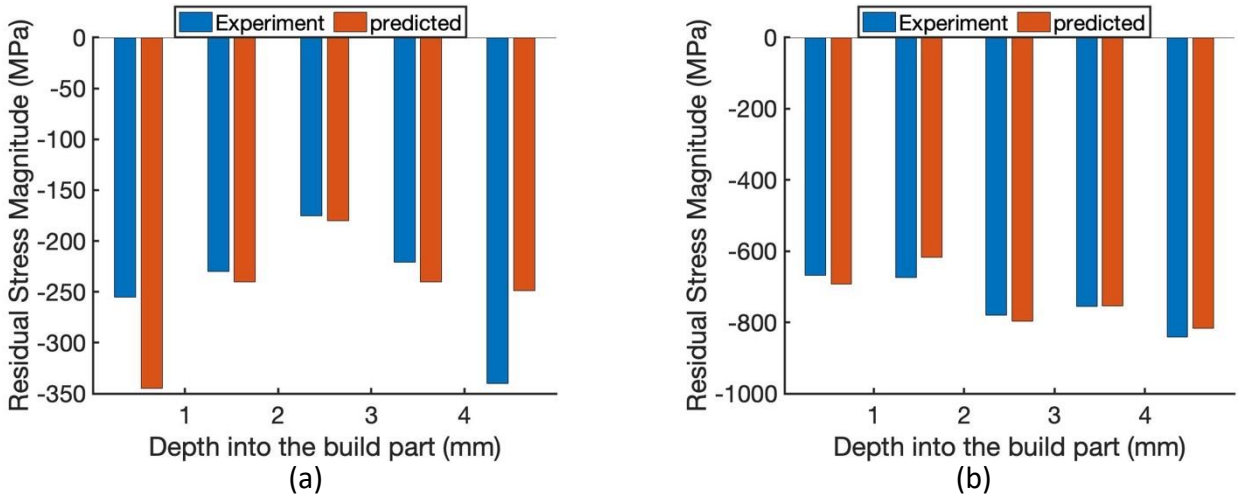

Figure 12*. Predicted and measured residual stress of 18Ni350 sample built via L-PBF with the laser power of 120 W and scan speed of 200 mm/s, layer thickness of 45 µm, hatching space of 100 µm, and scan pattern of unconnected zigzag; (a) along the scan direction ; (b) along the build direction.*

6. Conclusions

A physics-based analytical model is proposed to predict the residual stress in laser powder bed fusion process. Maraging Steel 350 is used as a material system example to validate the proposed model by measuring the residual stress of the fabricated samples via X-ray diffraction. The proposed thermo-mechanical analytical model predicts the temperature field of the additively manufactured part using moving point heat source approach by considering the effects of scan strategies, heat loss due to convection and radiation, and energy needed for solid-state phase change. The build part may experience high thermal stress due to the high-temperature gradient. The thermal stress is obtained using Green's function of stresses due to the point body load. The thermal stress may exceed the yield strength of the material. Thus, the Johnson-Cook flow stress model is used to determine the yield surface. Due to the cyclic heating and cooling, the material

experiences high residual stress. The residual stress is predicted using incremental plasticity and kinematic hardening behavior of the metal according to the property of volume invariance in plastic deformation in coupling with the equilibrium and compatibility conditions.
The Johnson-Cook parameters of maraging steel 350 are predicted using inverse analysis. In this approach, the modified chip formation model is used to predict the machining forces, and the iterative gradient search is used to determine the J-C parameters when the difference between predicted and measured cutting forces is below an acceptable low value.
The residual stress distributions in build depth is predicted along the scan direction and build direction under three different process conditions with various laser powers and scan speeds. The results showed that the residual stress is highly compressive in both directions since during the cooling cycle the heat-affected zone begins to cool down and the shrinkage of material in this zone tend to occur, but the shrinkage is restrained by the plastic strain formed during the heating stage, thus, the compressive stress state builds up in the solidified part.
Moreover, a comparison of the residual stress along the scan direction and build direction showed that the predicted residual stress along the build direction is higher than that along the scan direction. Different heat transfer mechanisms along the scan direction and build direction could contribute to this difference.
Results from the proposed analytical residual stress model showed good agreement with X-ray diffraction measurements used to determine the residual stresses in the maraging steel 350 specimens built via L-PBF. Thus, the proposed model is a valuable tool for the rapid and accurate prediction of the residual stress build-up in the parts built via L-PBF. Due to the high computational efficiency of the proposed model, this model can also be used for the real-time monitoring and control of the build process, and also optimization of the process parameters in achieving a high-quality part.

References

1. Bartlett, J.L. and X. Li, *An overview of residual stresses in metal powder bed fusion.* Additive Manufacturing, 2019.
2. King, W.E., et al., *Observation of keyhole-mode laser melting in laser powder-bed fusion additive manufacturing.* Journal of Materials Processing Technology, 2014. **214**(12): p. 2915-2925.
3. Khairallah, S.A., et al., *Laser powder-bed fusion additive manufacturing: Physics of complex melt flow and formation mechanisms of pores, spatter, and denudation zones.* Acta Materialia, 2016. **108**: p. 36-45.
4. Caiazzo, F., et al., *Laser powder-bed fusion of Inconel 718 to manufacture turbine blades.* The International Journal of Advanced Manufacturing Technology, 2017. **93**(9-12): p. 4023-4031.
5. Masoomi, M., S.M. Thompson, and N. Shamsaei, *Laser powder bed fusion of Ti-6Al-4V parts: Thermal modeling and mechanical implications.* International Journal of Machine Tools and Manufacture, 2017. **118**: p. 73-90.
6. Levkulich, N., et al., *The effect of process parameters on residual stress evolution and distortion in the laser powder bed fusion of Ti-6Al-4V.* Additive Manufacturing, 2019. **28**: p. 475-484.

7. Barros, R., et al., *Laser Powder Bed Fusion of Inconel 718: Residual Stress Analysis Before and After Heat Treatment.* Metals, 2019. **9**(12): p. 1290.
8. Tabei, A., et al., *Modeling of texture development in additive manufacturing of Ni-based superalloys.* The International Journal of Advanced Manufacturing Technology, 2019: p. 1-10.
9. Bandyopadhyay, A. and K.D. Traxel, *Invited review article: metal-additive manufacturing—modeling strategies for application-optimized designs.* Additive manufacturing, 2018. **22**: p. 758-774.
10. An, K., et al., *Neutron residual stress measurement and numerical modeling in a curved thin-walled structure by laser powder bed fusion additive manufacturing.* Materials & design, 2017. **135**: p. 122-132.
11. Yadroitsev, I. and I. Yadroitsava, *Evaluation of residual stress in stainless steel 316L and Ti6Al4V samples produced by selective laser melting.* Virtual and Physical Prototyping, 2015. **10**(2): p. 67-76.
12. Liu, Y., Y. Yang, and D. Wang, *A study on the residual stress during selective laser melting (SLM) of metallic powder.* The International Journal of Advanced Manufacturing Technology, 2016. **87**(1-4): p. 647-656.
13. Wu, A.S., et al., *An experimental investigation into additive manufacturing-induced residual stresses in 316L stainless steel.* Metallurgical and Materials Transactions A, 2014. **45**(13): p. 6260-6270.
14. Staub, A., A.B. Spierings, and K. Wegener, *Correlation of meltpool characteristics and residual stresses at high laser intensity for metal lpbf process.* Advances in Materials and Processing Technologies, 2019. **5**(1): p. 153-161.
15. Wang, Z., et al., *Residual stress mapping in Inconel 625 fabricated through additive manufacturing: Method for neutron diffraction measurements to validate thermomechanical model predictions.* Materials & Design, 2017. **113**: p. 169-177.
16. Hajializadeh, F. and A. Ince, *Finite element–based numerical modeling framework for additive manufacturing process.* Material Design & Processing Communications, 2019. **1**(1): p. e28.
17. Cheng, B. and K. Chou, *Geometric consideration of support structures in part overhang fabrications by electron beam additive manufacturing.* Computer-Aided Design, 2015. **69**: p. 102-111.
18. Siewert, M., et al., *Validation of Mechanical Layer Equivalent Method for simulation of residual stresses in additive manufactured components.* Computers & Mathematics with Applications, 2019. **78**(7): p. 2407-2416.
19. Garrison Jr, W. and M. Banerjee, *Martensitic non-stainless steels: high strength and high alloy.* 2016.
20. Viswanathan, U., G. Dey, and M. Asundi, *Precipitation hardening in 350 grade maraging steel.* Metallurgical Transactions A, 1993. **24**(11): p. 2429-2442.
21. Jaeger, J.C. and H.S. Carslaw, *Conduction of heat in solids*. 1959: Clarendon P.
22. Ning, J., et al., *Analytical modeling of 3D temperature distribution in selective laser melting of Ti-6Al-4V considering part boundary conditions.* Journal of Manufacturing Processes, 2019. **44**: p. 319-326.

23. Mirkoohi, E., et al., *Heat Source Modeling in Selective Laser Melting.* Materials, 2019. **12**(13): p. 2052.
24. Mirkoohi, E., et al., *Three-dimensional semi-elliptical modeling of melt pool geometry considering hatch spacing and time spacing in metal additive manufacturing.* Journal of Manufacturing Processes, 2019. **45**: p. 532-543.
25. Mirkoohi, E., et al., *Thermal modeling of temperature distribution in metal additive manufacturing considering effects of build layers, latent heat, and temperature-sensitivity of material properties.* Journal of Manufacturing and Materials Processing, 2018. **2**(3): p. 63.
26. Woo, W., et al., *Effect of interlayers and scanning strategies on through-thickness residual stress distributions in additive manufactured ferritic-austenitic steel structure.* Materials Science and Engineering: A, 2019. **744**: p. 618-629.
27. Saif, M., C. Hui, and A. Zehnder, *Interface shear stresses induced by non-uniform heating of a film on a substrate.* Thin Solid Films, 1993. **224**(2): p. 159-167.
28. Khan, A.S. and S. Huang, *Continuum theory of plasticity*. 1995: John Wiley & Sons.
29. McDowell, D., *An approximate algorithm for elastic-plastic two-dimensional rolling/sliding contact.* Wear, 1997. **211**(2): p. 237-246.
30. Jiang, Y. and H. Sehitoglu, *An analytical approach to elastic-plastic stress analysis of rolling contact.* TRANSACTIONS-AMERICAN SOCIETY OF MECHANICAL ENGINEERS JOURNAL OF TRIBOLOGY, 1994. **116**: p. 577-577.
31. Group, A.M., J. Merwin, and K. Johnson, *An analysis of plastic deformation in rolling contact.* Proceedings of the Institution of Mechanical Engineers, 1963. **177**(1): p. 676-690.
32. Ning, J. and S.Y. Liang, *Inverse identification of Johnson-Cook material constants based on modified chip formation model and iterative gradient search using temperature and force measurements.* The International Journal of Advanced Manufacturing Technology, 2019. **102**(9-12): p. 2865-2876.
33. Yu-Lung Lo, B.-Y.L., Hong-Chuong Tran *Optimized Hatch Space Selection in Double-Scanning Track Selective Laser Melting Process* The International Journal of Advanced Manufacturing Technology, 2019.
34. Hong-Chuong Tran, Y.-L.L., *Systematic Approach for Determining Optimal Processing Paramters to Produce Parts with High Density in Selective Laser Melting Process* The International Journal of Advanced Manufacturing Technology, 2019.
35. Tran, H.-C. and Y.-L. Lo, *Heat transfer simulations of selective laser melting process based on volumetric heat source with powder size consideration.* Journal of Materials Processing Technology, 2018. **255**: p. 411-425.
36. Tran, H.-C., Y.-L. Lo, and M.-H. Huang, *Analysis of Scattering and Absorption Characteristics of Metal Powder Layer for Selective Laser Sintering.* IEEE/ASME Transactions on Mechatronics, 2017. **22**(4): p. 1807-1817.
37. Nadammal, N., et al., *Influence of support configurations on the characteristics of selective laser-melted inconel 718.* JOM, 2018. **70**(3): p. 343-348.
38. Prevey, P.S., *X-ray diffraction residual stress techniques.* ASM International, ASM Handbook., 1986. **10**: p. 380-392.

39. Viswanathan, U., G. Dey, and V. Sethumadhavan, *Effects of austenite reversion during overageing on the mechanical properties of 18 Ni (350) maraging steel.* Materials Science and Engineering: A, 2005. **398**(1-2): p. 367-372.
40. Ganeriwala, R., et al., *Evaluation of a thermomechanical model for prediction of residual stress during laser powder bed fusion of Ti-6Al-4V.* Additive Manufacturing, 2019. **27**: p. 489-502.